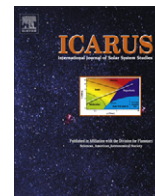




Contents lists available at ScienceDirect

Icarus

journal homepage: [www.elsevier.com/locate/icarus](http://www.elsevier.com/locate/icarus)

## Optimal dynamos in the cores of terrestrial exoplanets: Magnetic field generation and detectability

Peter Driscoll<sup>a,b,\*</sup>, Peter Olson<sup>a</sup>

<sup>a</sup> Earth & Planetary Sciences, Johns Hopkins University, MD 21218, United States

<sup>b</sup> Geology & Geophysics, Yale University, CT 06511, United States

### ARTICLE INFO

#### Article history:

Received 29 April 2010

Revised 1 February 2011

Accepted 10 February 2011

Available online xxx

#### Keywords:

Extrasolar planets

Geophysics

Interiors

Magnetic fields

Radio observations

### ABSTRACT

A potentially promising way to gain knowledge about the internal dynamics of extrasolar planets is by remote measurement of an intrinsic magnetic field. Strong planetary magnetic fields, maintained by internal dynamo action in an electrically conducting fluid layer, are helpful for shielding the upper atmosphere from stellar wind induced mass loss and retaining water over long (Gyr) time scales. Here we present a whole planet dynamo model that consists of three main components: an internal structure model with composition and layers similar to the Earth, an optimal mantle convection model that is designed to maximize the heat flow available to drive convective dynamo action in the core, and a scaling law to estimate the magnetic field intensity at the surface of a terrestrial exoplanet. We find that the magnetic field intensity at the core surface can be up to twice the present-day geomagnetic field intensity, while the magnetic moment varies by a factor of 20 over the models considered. Assuming electron cyclotron emission is produced from the interaction between the stellar wind and the exoplanet magnetic field we estimate the cyclotron frequencies around the ionospheric cutoff at 10 MHz with emission fluxes in the range  $10^{-4}$ – $10^{-7}$  Jy, below the current detection threshold of radio telescopes. However, we propose that anomalous boosts and modulations to the magnetic field intensity and cyclotron emission may allow for their detection in the future.

© 2011 Elsevier Inc. All rights reserved.

### 1. Introduction

There is evidence of a large scale magnetic field maintained by internal dynamo action for every planet in the Solar System with the possible exception of Venus. In addition, magnetic fields have been measured on several satellites, but only Ganymede's field is likely to be generated by internal dynamo action. Detection of terrestrial exoplanet dynamos would provide important constraints on internal structures, dynamics, energetics, and the ubiquity of planetary magnetic fields in general. Dynamo action is maintained by efficient heat transfer from the deep interior so that planets with strong magnetic fields may also imply mobile-lid mantle convection. Furthermore, maintaining a habitable surface over long time scales may require a magnetic field to shield the atmosphere from mass loss, retain large amounts of water, and protect the surface from charged particles (Dehant et al., 2007; Lammer et al., 2007). Therefore, the search for terrestrial exoplanet magnetic fields is a critical component of the search for habitable planets.

Without a large scale planetary magnetic field, charged particles interact directly with the upper atmosphere and accelerate

atmospheric mass loss. More frequent stellar flares and increased stellar wind flux associated with an active young star amplify these effects during the early stages of planetary evolution. Earth's strong magnetic field shields the atmosphere, promoting the retention of large amounts of water over geologic time scales. This may not have been the case for the other terrestrial planets. For example the measured D/H ratio in the venusian atmosphere indicates that it had more water in the past (Lammer et al., 2008), consistent with the absence of a strong magnetic field. Also, since maintenance of a strong magnetic field in a terrestrial planet likely requires large scale mantle convection, planets with strong magnetic fields may also maintain mobile-lid surface tectonics. Evidence for this coupling exists for both Venus and Mars, where some form of active surface tectonics may have ceased in conjunction with the extinction of dynamo action in their core and loss of water from their surfaces (Nimmo, 2002; Stevenson, 2001).

More than 400 extrasolar planets have been detected to date, with 20 planets less massive than  $10M_E$  ( $M_E = 1$  Earth-mass) (Schneider, 2010). Although the diversity among extrasolar planets has been surprising (Fischer, 2008; Howard et al., 2010), the key ingredients to sustaining a dynamo, an energy source (i.e. convection), rotation, and a large volume of electrically conducting fluid, are thought to be common planetary phenomenon. Numerical simulations indicate that planets in the 1– $10M_E$  regime with an

\* Corresponding author at: Geology & Geophysics, Yale University, CT 06511, United States.

E-mail address: [peter.driscoll@yale.edu](mailto:peter.driscoll@yale.edu) (P. Driscoll).

Earth-like (terrestrial) composition that harbor large, mostly iron cores form readily within 3 AU of their host star (Laughlin et al., 2004; Ida and Lin, 2004), and are often referred to as “super-Earths”. In this paper we explore the possibility of detecting the magnetic field of such a planet.

The magnetic planets in the Solar System emit intense electron cyclotron radiation at radio frequencies (1–100 MHz), which is generated by energetic solar wind electrons interacting with the planetary magnetic field. Cyclotron emission is modulated at the rotation period of the planet if the magnetic field contains non-axisymmetric components and has been used to estimate the rotation periods of the giant planets (e.g. Anderson and Schubert, 2007; Zarka et al., 2001). Massive extrasolar planets with strong magnetic fields are expected to produce detectable cyclotron emission at radio frequencies (Zarka, 2007), but little attention has been paid to the potential emission from terrestrial exoplanets. Several other techniques have been proposed to infer the presence of exoplanet magnetic fields, and evidence of the interaction between the magnetic field of the star and planet has been claimed in about 10 (e.g. Shkolnik et al., 2008).

Our main goal is to explore the detectability of low mass, terrestrial exoplanet magnetic fields. This requires a number of important assumptions because the likely internal structure and thermal evolution of terrestrial exoplanets is unknown. The first models of radial variation of density in planets with end member compositions were constructed in the pioneering work of Zapolsky and Salpeter (1969). More recently preliminary internal structure models of super-Earths have been constructed to obtain simple scaling laws for the planetary and core radius as a function of planetary mass (e.g. Valencia et al., 2006; Seager et al., 2007; Sotin et al., 2007). These models either ignore the thermal state of the mantle and core and phase transitions therein or assume a core-mantle boundary (CMB) heat flux proportional to planet mass. Exoplanets may have important differences from the terrestrial planets in the Solar System, therefore we focus on optimizing a potentially observable feature of terrestrial exoplanets: their magnetic field. The most promising targets are those with extremely intense magnetic fields, likely maintained by efficient heat transfer out of the core. We compute internal structure profiles and develop a thermal convection model that maximizes core heat flow, which we refer to as the optimal state for dynamo action.

Before introducing the specifics of the model it is helpful to list the main assumptions and idealizations of the optimal model. We assume an Earth-like composition, structure, surface temperature and pressure, and rotation rate. We assume the mantle and core are convecting rigorously, and that there is no large scale melting in the mantle. We propose that as the planet cools it may pass through an optimal state for dynamo action before evolving into a sub-optimal state, perhaps similar to the present-day Earth.

We describe the internal structure model in Section 2, the optimal thermal model in Section 3, and magnetic field generation in Section 4. The main results are presented in Section 5, and considerations of magnetic field detectability are in Section 6. Finally, we summarize our main conclusions and discuss the prospects for detecting an exoplanet magnetic field in the near future in Section 7.

## 2. Internal structure model

The internal structure modeling technique employed here is very similar to those of Valencia et al. (2006), Sotin et al. (2007) and Seager et al. (2007). The following set of equations are solved in a spherical shell of thickness  $dr$  and are then integrated over the full radius of the planet  $R$  subject to boundary conditions. The continuity equation describing the change in mass  $m(r)$  within radius

$r$ , Poisson’s equation for gravity  $g$ , the hydrostatic equation for pressure  $P$ , and the Adams–Williamson equation for density  $\rho$  are,

$$dm(r)/dr = 4\pi r^2 \rho(r) \quad (1)$$

$$dg(r)/dr = 4\pi G \rho(r) - 2Gm(r)/r^3 \quad (2)$$

$$dP(r)/dr = -\rho(r)g(r) \quad (3)$$

$$d\rho(r)/dr = -\rho^2(r)g(r)/K_S(r) \quad (4)$$

where  $K_S(r) = \rho(\partial P/\partial \rho)_S$  is the isentropic bulk modulus and  $G$  is the gravitational constant. We write  $K_S$  in terms of the isothermal bulk modulus  $K_T$  as,

$$K_S(r) = K_T(r)[1 + \alpha(r)\gamma(r)T(r)] \quad (5)$$

where  $\alpha$  is thermal expansivity,  $\gamma$  is the Gruneisen parameter, and  $T$  temperature. The equation of state (EOS) we use to relate  $K_T$  to  $\rho$  is the third order Vinet EOS (Oganov, 2007; Vinet et al., 1989),

$$K_T = K_0 x^{-2/3} [1 + (1 + \theta x^{1/3})(1 - x^{1/3})] \exp[\theta(1 - x^{1/3})] \quad (6)$$

where the zero subscript refers to the zero pressure value of a quantity,  $x(r) = \rho(r)/\rho_0$ , and  $\theta = 3/2(K'_0 - 1)$ , where  $K'_0$  is the zero pressure derivative of  $K_T$ . The adiabatic temperature gradient,

$$dT_{ad}(r)/dr = -\rho(r)g(r)\gamma(r)T(r)/K_S(r) \quad (7)$$

describes the increase in temperature with depth in a well-mixed layer. The depth-dependence of the remaining thermodynamic parameters  $\gamma$  and  $\alpha$  are parameterized by

$$\gamma(r) = \gamma_0(x(r))^{-\gamma_1}, \quad \alpha(r) = \alpha_0(x(r))^{-\alpha_2} \quad (8)$$

where  $\gamma_0$ ,  $\gamma_1$ , and  $\alpha_0$  are constant within each compositional layer (Table 1). The variation of  $\alpha$  with density in (8) is based on high pressure experiments (Chopelas and Boehler, 1992; Merkel et al., 2000).

We impose surface conditions on each model of  $P_0 = 1$  atm,  $\rho_0 = 3226$  kg m<sup>-3</sup>, and  $T_0 = 300$  K. Conditions at the center ( $r = 0$ ) of each model require that the mass and gravity go to zero and the other variables (e.g.  $\rho$  and  $T$ ) remain smooth and finite. The internal structure Eqs. (1)–(8) are integrated from the surface inwards and the surface radius  $R$  is modified until the conditions are satisfied at the center, with a typical error in  $R$  that corresponds to about one part in  $10^4$ .

### 2.1. Layers

We include up to five layers in the model: a peridotite upper mantle, a perovskite mid-mantle, a post-perovskite lower mantle, and a solid or liquid metallic core. We do not include a spinel structure as in the transition zone of the Earth’s mantle, because this layer is less than 300 km thick. There are four possible transitions or discontinuities: peridotite to perovskite, perovskite to post-perovskite in the mantle, a core–mantle boundary (CMB) where the material changes from silicates to iron, and an iron solidus boundary denoted the inner core boundary (ICB). The pressure at which the olivine transitions to perovskite (in the spinel structure) is a function of temperature described by Ito and Takahashi (1989)

$$P(T) = P_{pd0} - \gamma_{pd}T \quad (9)$$

where the reference pressure is  $P_{pd0} = 28.3$  GPa and the Clapeyron slope is  $\gamma_{pd} = 2.8$  MPa K<sup>-1</sup>. The pressure at which perovskite transforms to the higher density post-perovskite phase is described by

$$P(T) = P_{ppv0} + \gamma_{ppv}(T - T_{ppv0}) \quad (10)$$

where the reference pressure and temperature are  $P_{ppv0} = 124$  GPa and  $T_{ppv0} = 2500$  K, and the Clapeyron slope is  $\gamma_{ppv} = 8$  MPa K<sup>-1</sup> (Hernlund and Labrosse, 2007).

**Table 1**

Material constants of each layer. Constants for peridotite (olivine) and perovskite are similar to those of [Stixrude and Lithgow-Bertelloni \(2005\)](#). Constants for post-perovskite are similar to those of [Shim \(2008\)](#). Constants for liquid and solid Fe are similar to those of [Stacey and Davis \(2004\)](#), [Lin et al. \(2003\)](#), [Uchida et al. \(2001\)](#) and [Boehler et al. \(1990\)](#). Non-dimensional quantities are denoted (n.d.).

Parameter	Peridotite	Perovskite	Post-perovskite	Liquid Fe	Solid Fe
$\rho_0$ (kg m <sup>-3</sup> )	3226	4000	4100	6900	7300
$K_0$ (GPa)	128	200	231	125	165
$K'_0$ (n.d.)	4.2	4.0	4.0	5.5	4.9
$\gamma_0$ (n.d.)	0.99	1.0	1.5	1.60	1.60
$\gamma_1$ (n.d.)	2.1	1.4	1.4	0.92	0.92
$\alpha_0$ ( $\times 10^{-6}$ K <sup>-1</sup> )	20	20	20	40	40

The core–mantle boundary  $r_{cmb}$  is defined as the radius at which the mass above  $r_{cmb}$  is equal to the mantle mass  $M_m = M(1 - \text{CMF})$ , where  $M$  is the total planet mass and we prescribe a core-mass fraction (CMF) of either 0.32 (Earth-like) or 0.65 (Mercury-like). The iron core can be completely molten, completely solid, or partially molten with a liquid or solid shell depending on where the core temperature profile intersects the iron solidus. We define the iron solidus by Lindemann's Law ([Poirier, 1991](#))

$$T_{melt} = T_{Fe0} \exp[2\gamma_0(1 - 1/x) + 2/3 \ln(1/x)] \quad (11)$$

where  $T_{Fe0} = 1811$  K is the zero pressure melting temperature of iron ([Weast, 2009](#)) and  $\gamma\rho \approx \gamma_0\rho_0$ . Depending on the relative slopes of the core geotherm and the iron melting curve, the core may have a liquid shell with a solid inner core as in the Earth, or vice versa, or the core may be entirely liquid or solid. We note that the assumed differentiation of iron cores in terrestrial exoplanets has recently been questioned on the basis that if the iron is either oxidized in primitive planetesimals or the iron lingers long enough to oxidize during a magma ocean phase before gravitational instability sets in, then core segregation may not occur at all ([Elkins-Tanton and Seager, 2008](#)). However, oxidation is more likely on small planetary bodies where temperatures are cooler during the formation phase and iron-rich impactors are disaggregated into small, centimeter scale fragments.

## 2.2. Material properties

With four possible discontinuities there are five distinct layers. The thermodynamic properties of the candidate materials, which can be discontinuous across boundaries, are uncertain despite the constraints provided by high pressure experiments. As a consequence of these large uncertainties, seismically consistent Earth structure models have been constructed over a range of parameter values. We use a set of zero pressure constants, shown in [Table 1](#), that produce an Earth model internal structure similar to the preliminary Earth reference model (PREM) by [Dziewonski and Anderson \(1981\)](#) and the geotherm constructed by [Stacey \(1992\)](#). More recent estimates of the core melting curve by [Alfe et al. \(2003\)](#) suggest that temperatures may be  $\sim 600$  K hotter than the ICB temperature of 5000 K estimated by [Stacey \(1992\)](#).

The thermal conductivity in the mantle is assumed to vary with pressure as [Van den Berg et al. \(2002\)](#),

$$k = k_0(1 + PK'_0/K_0) \quad (12)$$

where  $k_0 = 3.3$  W K<sup>-1</sup> m<sup>-1</sup>, which closely approximates the model of [Hofmeister \(1999\)](#). The adiabatic heat flow out of the core depends on the thermal conductivity of iron and thermal gradient at the top of the core. For core thermal conductivity we use the Wiedemann–Franz Law  $k = \sigma LT$  where  $\sigma = 3 \times 10^5$  S m<sup>-1</sup> is the assumed electrical conductivity of the outer core,  $L = 2.5 \times 10^{-8}$  W S<sup>-1</sup> K<sup>-2</sup> is the Lorentz Number ([Poirier, 1991](#); [Stacey and Loper, 2007](#)), and  $T$  is the absolute temperature.

## 3. Thermal model

Seismically inferred estimates of Earth's CMB heat flow  $\sim 10 \pm 4$  TW ([Lay et al., 2006](#); [Van der Hilst et al., 2007](#)) are larger than estimates of the core adiabatic heat flow  $\sim 3$ – $4$  TW, implying that convection in the outer core is driven at least in part by thermal gradients. Previous internal structure models of super-Earths have imposed simplified thermal profiles that assume temperature jumps in the boundary layers similar to the Earth (e.g. [Valencia et al., 2006](#); [Sotin et al., 2007](#)), or alternatively have ignored any non-adiabatic thermal contribution since it has a minor influence on the planetary radius and density (e.g. [Seager et al., 2007](#)). In this section we describe a whole planet thermal model that reproduces a geotherm for the Earth and produces optimal thermal profiles for a range of masses and CMFs that maximize the core heat flow.

A detailed comparison of the influences of all possible core energy sources on the dynamo magnetic field strength is beyond the scope of this paper, as their many interactions are hardly known. The primary effects that draw energy from the core are cold downwellings and hot upwellings in the mantle, and our model seeks to maximize these agents. We focus on thermal convection for several reasons: Thermal convection likely occurs at some point in all planetary cores because of initial conditions. Compositional convection complements thermal convection, but a high compositional buoyancy flux implies that the core is solidifying quickly, which will decrease the volume of conducting fluid and the depth of the dynamo region. In addition, a large compositional buoyancy flux will be temporary and ultimately lead to complete solidification of the core. Mathematically, radioactive heating in the core appears like a secular cooling term in the heat equation, which we do include. External driving, such as precession and tidal forcing, add only incrementally to convection when present simultaneously ([Lavorel and Le Bars, 2010](#)).

The fundamental assumption of the thermal model is that the mantle cools the core as fast as possible. In terrestrial type planets the mantle determines the steady-state heat flux both at the surface of the planet and at the CMB. The rate at which heat is extracted from the core is limited by the lowermost mantle boundary layer, the D' layer in the Earth, in at least two ways: the thermal conductivity is probably much lower than that of the iron rich core, and the temperature gradient across the layer is controlled by slow convective processes in the mantle. The mantle cooling rate is limited by the efficiency of heat conduction through the upper mantle thermal boundary layer. We seek to maximize this efficiency. Therefore, to estimate the end member case of maximum core heat flow we will focus on models with negligible internal heating, so that all the heat lost from the mantle originates from the core. [Section 5.6](#) considers the influence of internal heating in the mantle on the magnetic field intensity.

To investigate the most energetically favorable, or optimal thermal state, it is assumed that both the mantle and core are convecting vigorously, such that within each convective region away from boundary layers the material is well-mixed and the temperature

gradient is adiabatic. Temperature jumps at each boundary layer are determined by assuming the temperature at the base of the thermal boundary layer reaches the local solidus. If the thermal boundary layer temperature is substantially below the solidus then heat flow will be sub-optimal. If the average geotherm exceeds the mantle solidus then substantial melting occurs, excess heat is quickly advected to the surface, and eventually the boundary layer returns to a stable, slightly sub-solidus temperature. Although this simplification requires that the average geotherm be sub-solidus, it does not rule out localized thermal perturbations.

### 3.1. Mantle temperatures

For convenience we separate the mantle temperature profile  $T(r)$  into a super-adiabatic (convective) component  $T_{conv}$  and adiabatic correction  $T_{ad}$  so that  $T(r) = T_{conv}(r) + T_{ad}(r)$ . In thermal boundary layers conduction is the dominant mechanism for heat transfer so we use the error function solution to the heat equation to describe the temperature profiles in the upper and lower mantle,

$$T_1(r) = T_0 + \Delta T_1 \operatorname{erf}\left(\frac{R-r}{\delta_1}\right), \quad \text{for } r_{mid} \leq r \leq R \quad (13)$$

$$T_2(r) = T_{mid} + \Delta T_2 \operatorname{erfc}\left(\frac{r-r_{cmb}}{\delta_2}\right), \quad \text{for } r_{cmb} \leq r \leq r_{mid} \quad (14)$$

where the subscripts 1 and 2 refer to the upper and lower mantle thermal boundary layers, respectively,  $r_{mid}$  is the mid-mantle radius,  $\Delta T_1 = (T_{mid} - T_0)$  and  $\Delta T_2 = (T_{cmb} - T_{mid})$  are the boundary layer temperature jumps, and  $\delta$  is the thermal boundary layer thickness. The temperature at the mid-mantle is  $T_{mid}$  and at the CMB is  $T'_{cmb} = T_{cmb} - T_{ad,cmb}$ , where  $T_{ad,mid}$  is the adiabatic temperature contribution at the mid-mantle, so that  $T_{mid}$  and  $T'_{cmb}$  have the adiabat removed. The convective temperature profile is then given by  $T_{conv}(r) = T_1(r) + T_2(r)$ , so that  $T_{conv} = T_1 = T_2$  at  $r_{mid}$ .

To specify the mantle geotherm we solve for the unknown variables  $T'_{cmb}$ ,  $T_{mid}$ ,  $\delta_1$ , and  $\delta_2$  in (13) and (14) subject to three dynamical constraints: (i) the local Rayleigh number is critical for convection at the base of the upper mantle thermal boundary layer; (ii) the upper and lower mantle thermal boundary layer profiles are at the local solidus temperature; (iii) the core heat flow is equal to the planetary surface heat flow. We refer to models that meet these three dynamical constraints as in the *optimal state for thermal convection in the core*. The method to solve for the remaining unknowns by applying these constraints to the thermal boundary layers in (13) and (14) is described below.

### 3.2. Mantle solidus

To specify the melting temperature throughout the mantle as a function of pressure we use the mantle solidus for the two major mantle constituents in this model: peridotite and perovskite. The dry peridotite melting curve derived from a compilation of piston cylinder and multianvil experiments (Hirschmann, 2000) is approximated by

$$T_{melt} = T_{pd0} + 90P, \quad \text{for } P < 16 \text{ GPa} \quad (15)$$

where  $P$  is in GPa,  $T$  is in K, and  $T_{pd0} = 1373$  K. The melting curve for perovskite in the lower mantle (Zerr et al., 1998; Oganov, 2007) is approximated by

$$T_{melt} = T_{pv0} + 400(P - 5)^{1/2}, \quad \text{for } P > 16 \text{ GPa} \quad (16)$$

where  $P$  is in GPa and  $T_{pv0} = 1500$  K. The two curves are constructed to give the same melting temperature at 16 GPa.

### 3.3. Optimal state

In the optimal models CMB temperature is set to the mantle melting temperature,  $T_{cmb} = T_{melt}(P_{cmb})$ . The Earth model uses the presently preferred value of  $T_{cmb} = 4000$  K. An otherwise similar model that allows the lower most mantle to be at the perovskite melting temperature of  $T_{cmb} \approx 6000$  K is referred to as the optimal Earth-mass model. This may be representative of the early Earth when  $T_{cmb}$  was just below the silicate solidus following magma ocean solidification.

The assumption that the lower mantle is made up of only perovskite, with no (Fe,Mg)O, has implications for the melting temperature at the CMB. High pressure experiments and theoretical ab initio calculations of the melting properties of MgO at CMB pressures indicates melting begins around 5500 K, and is substantially less than the solidus of perovskite at these pressures (Boehler, 2007). Furthermore, eutectic melting may occur at even lower temperatures of  $\sim 4300$  K (Holland and Ahrens, 1997). Recently it has been proposed that a thin (Fe,Mg)O melt layer at the base of the mantle may be negatively buoyant compared to the surrounding solid lower mantle and therefore dynamically stable (Mosenfelder et al., 2007). Modifying the solidus curve of the lower mantle in (16) will not change the optimal core heat flow  $Q_c$  calculated below because  $Q_c$  is related to the upper mantle boundary layer heat flow, which is determined by the better constrained upper mantle peridotite solidus in (15). A substantial decrease of  $T_{cmb}$  combined with a fast core cooling rate may lead to complete solidification of the core and extinction of the dynamo.

The mid-mantle temperature defined in (13) and (14) is limited by the shape of the error function describing the thermal boundary layers and the mantle solidus. We define the depth at which the upper mantle temperature profile  $T_1$  touches the silicate melting curve  $T_{melt}$  as  $z_{melt}$ . In general, this depth could be a fraction of the thermal boundary layer thickness so that  $z_{melt} = \xi \delta_1$ , where  $\xi$  is between 0 and 1. A small  $\xi$  implies that the solidus crossing occurs close to the surface, producing a larger region of partial melt. For simplicity we choose  $\xi = 1$  so that  $z_{melt} = \delta_1$ , which produces a thin layer of partial melt just below  $z_{melt}$  due to the shape of the error function (Fig. 1). To solve for  $z_{melt}$  we set  $T_1(z_{melt}) = T_{melt}(z_{melt})$  giving,

$$T_{mid}(z_{melt}) = T_0 + \frac{1}{\operatorname{erf}\xi} [T_{melt}(z_{melt}) - T_{ad}(z_{melt}) - T_0] \quad (17)$$

where we have used (13) and (14) and  $\Delta T_1 = T_{mid} - T_0$ . To determine  $z_{melt}$  we invoke dynamical constraint (i) requiring that  $Ra(\delta_1) = Ra_{crit}$ ,

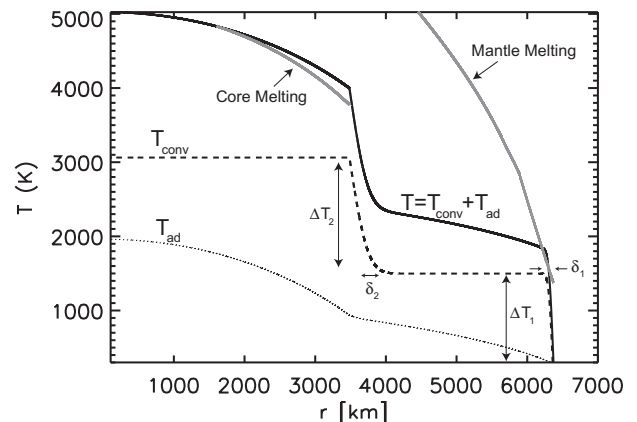


**Fig. 1.** Temperature profile for the Earth model (solid black). Mantle and core solidus (grey), convective profile (dashed) and adiabatic profile (dotted). Labeled are temperature jumps ( $\Delta T$ ) and depths ( $\delta$ ) of the upper (1) and lower (2) mantle thermal boundary layers.

where  $Ra_{crit} = 660$  (Turcotte and Schubert, 2002). The Rayleigh number is defined as

$$Ra = \frac{\alpha g \Delta T \delta^3}{\kappa \nu} \quad (18)$$

where  $\Delta T$  is the temperature jump across the depth interval  $\delta$ . We use a thermal diffusivity of  $\kappa = 10^{-6} \text{ m}^2 \text{ s}^{-1}$  and a dynamic viscosity of  $\eta = 2 \times 10^{20} \text{ Pa s}$  consistent with models of post-glacial rebound (Paulson et al., 2005), corresponding to a kinematic viscosity of  $\nu = \eta/\rho_0 = 6.2 \times 10^{16} \text{ m}^2 \text{ s}^{-1}$ . Although the viscosity is highly temperature dependent we use the viscosity at the base of the lithosphere where  $\delta = z_{melt}$  and  $Ra = Ra_{crit}$ . It has been shown that convective instabilities in the form of drips can develop in this region over millions of years (Conrad and Molnar, 1999). The viscosity is the same for all models because they have uniform composition, surface conditions, and contain a region of partial melt beneath the solidus crossing at  $Ra = Ra_{crit}$ .

Eqs. (17) and (18) each give a relation for  $\Delta T_1$  as a function of  $\delta_1$ , and their intersection provides a unique solution for both parameters. The convective temperature jump in the lower mantle thermal boundary layer to go from the mid-mantle to the CMB is then given by  $\Delta T_2 = T'_{cmb} - T_{mid}$ .

### 3.4. Heat flow

The conductive heat flow through the upper and lower mantle thermal boundary layers are, respectively,

$$Q_1 = \frac{2}{\sqrt{\pi}} A_1 k_1 \frac{\Delta T_1}{\delta_1}, \quad Q_c = \frac{2}{\sqrt{\pi}} A_2 k_2 \frac{\Delta T_2}{\delta_2} \quad (19)$$

where  $A_1$  and  $A_2$  are the areas of the planet surface and CMB, respectively,  $k_1$  and  $k_2$  are the thermal conductivities in the mantle at these boundaries, and the numerical factor  $2/\sqrt{\pi}$  comes from the derivative of the error function. We separate the total surface heat flow into two sources:

$$Q_1 = Q_R + Q_c \quad (20)$$

where  $Q_R$  is internal heat production in the mantle and  $Q_c$  is core heat flow (19). We note that secular cooling and radioactivity are included in  $Q_R$  because they can be written as volumetric source terms in the mantle energy balance. In the Earth model the radioactive heat production rate  $H$  (units of  $\text{W kg}^{-1}$ ) is specified, so  $Q_R = HM_m$ , where  $M_m$  is the mass of the mantle. For a given heat production rate and surface heat flow, the core heat flow  $Q_c$  is determined by (20).

Given  $Q_c$  and  $\Delta T_2$  we solve for the lower mantle boundary layer thickness from (19),

$$\delta_2 = \frac{2}{\sqrt{\pi}} A_2 k_2 \frac{\Delta T_2}{Q_c} \quad (21)$$

We now have all the thermal boundary layer properties needed to construct the whole planet temperature profiles using (7), (13), and (14) and to calculate the surface and core heat flows using (19).

### 3.5. Earth model

To construct a whole planet thermal profile for the present-day Earth, these steps are slightly modified as follows. The radioactivity of the continental crust is subtracted from the total surface heat flow because it does not enter into the mantle dynamics. This gives  $Q_1 = 40 \text{ TW}$  for the surface mantle heat flow. We assume a CMB temperature  $T_{cmb} = 4000 \text{ K}$  and a radioactive heat production density in the mantle  $H = 7.5 \times 10^{-12} \text{ W kg}^{-1}$ . Given the mass of the Earth's mantle, this implies a total internal heat generation of  $Q_R \approx 30 \text{ TW}$ , so that  $Q_c \approx 10 \text{ TW}$  from (20). We note that a recent estimate by Jaupart et al. (2007) actually partitions the mantle heat

loss of 30 TW into a radioactive heat generation of 13 TW and secular cooling of 17 TW. The critical Rayleigh number condition is not needed to solve this system, although its Rayleigh number is in fact close to the critical value. The remaining unknowns are then found the same way as the optimal model described above.

Fig. 1 shows the temperature profile of the Earth model (solid black), the mantle and core solidus defined in (15), (16) and (11) (grey), the convective profile  $T_{conv}$  defined by (13) and (14) (dashed), and the adiabatic correction defined in (7) (dotted). For the Earth model with  $\xi = 1$  we find  $z_{melt} = \delta_1 = 71.2 \text{ km}$ ,  $\Delta T_1 = 1498 \text{ K}$ ,  $Q_1 = 39.9 \text{ TW}$ ,  $Q_R = 30.2 \text{ TW}$ ,  $\delta_2 = 286 \text{ km}$ ,  $\Delta T_2 = 1564 \text{ K}$ ,  $Q_c = 9.7 \text{ TW}$ ,  $Q_{ad} = 2.4 \text{ TW}$ , and  $Q_{conv} = 7.2 \text{ TW}$ . Given these values the Rayleigh number in the upper thermal boundary layer is  $Ra_1 = 1342$ .

## 4. Magnetic field generation

### 4.1. Magnetic field scaling law

The onset of dynamo action in a convecting and electrically conductive fluid is an instability analogous to the onset of convection that occurs as the Rayleigh number is increased beyond a critical value, which depends on system parameters such as the rotation rate and the magnetic diffusivity. Generally, self-sustained magnetic field generation occurs in rapidly rotating convection when the magnetic Reynolds number of the flow  $Rm = \nu D/\eta_m$  exceeds a critical value of  $Rm_{crit} \simeq 40$ , where  $D$  is shell thickness and  $\eta_m$  is magnetic diffusivity (Roberts, 2007). Later we show, for reasonable rotation rates, that all of the models considered are supercritical for both convection and dynamo action.

Relating the magnetic field intensity of the dynamo to physical properties of the convecting fluid is challenging and a number of scaling laws have been proposed (e.g. Olson et al., 2009; Griessmeier et al., 2004). An early proposal by Elsasser (1946) was that the dynamo-generated magnetic field saturates at an intensity that is determined by an equilibration between the Coriolis and Lorentz forces, known as a magnetostrophic balance. This balance holds when the Elsasser number  $A = \sigma B^2/\rho\Omega$  is of order one, where  $\sigma$  is electrical conductivity and  $\Omega$  is planetary rotation rate. Sanchez-Lavega (2004) used the Elsasser number to predict the magnetic field intensity of giant extrasolar planets, and Griessmeier et al. (2004) used this and other scaling laws to estimate the extent to which the magnetic field of a hot jupiter might influence atmospheric loss rates. However, despite the importance of the magnetostrophic balance in dynamos, it is known that  $A$  varies by over an order of magnitude for the magnetic planets in the Solar System, with dipole based values of  $A \sim 5 \times 10^{-2}$  for the Earth and Jupiter and  $A \sim 10^{-3}$ – $10^{-5}$  for the other magnetic planets (Olson and Christensen, 2006). In addition, the Elsasser number criteria is at odds with numerical dynamo results, which show that the intensity of a convectively generated magnetic field becomes independent of the rotation rate in the limit of fast rotation.

Recently it has been proposed that a single magnetic field scaling law that is proportional to the energy flow through the dynamo region of the form  $B \propto (DF)^{1/3}$ , where  $D$  is dynamo region shell thickness and  $F$  is buoyancy flux, can be used to estimate the dipole magnetic field intensities of the planets in the Solar System, fast rotating M stars, and numerical dynamo models over an enormous range of parameters (Christensen and Aubert, 2006; Christensen et al., 2008, 2009). The exponential dependence of  $1/3$  can be derived from a simple dimensional analysis, assuming independence of the diffusivities and rotation rate. The balance of advection and Lorentz force terms in the conservation of momentum gives a relation between the Alfvén velocity and magnetic field,  $v_A \sim B/\sqrt{\rho\mu_0}$ . The unique relationship between  $v_A$  in units of  $[\text{m s}^{-1}]$ ,  $F$  in units of

[ $\text{m}^2 \text{s}^{-3}$ ], and  $D$  in units of [m], is  $v_A \sim (DF)^{1/3}$ . The success of this scaling law in predicting magnetic field strengths over many orders of magnitude demonstrates that magnetic field intensity is determined by the energy flux through the dynamo region and that it cannot grow indefinitely with rotation rate. The rotation rates of the dipolar-dominant magnetic planets in the Solar System, specifically Earth, Jupiter, and to a lesser extent Saturn, are sufficient for this law to apply.

We adopt a form of this scaling law from [Olson and Christensen \(2006\)](#) for the rms dipole field intensity at the CMB, modified to include entirely liquid cores,

$$B_c = \gamma_d (\rho \mu_0)^{1/2} (r_{\text{cmb}} F)^{1/3} \quad (22)$$

where  $\gamma_d = 0.2$  is the saturation constant for fast rotating dipolar dynamos,  $\mu_0 = 4\pi \times 10^{-7} \text{ H m}^{-1}$  is magnetic permeability,  $F = \alpha g q_{\text{conv}} / \rho c_p$  is the buoyancy flux, and  $q_{\text{conv}}$  is the convective heat flux. Substituting for  $F$  gives,

$$B_c = \gamma_d (\rho \mu_0)^{1/2} \left( \frac{\alpha g}{\rho c_p} r_{\text{cmb}} q_{\text{conv}} \right)^{1/3} \quad (23)$$

The rms dipole field intensity at the core surface is projected to the planet surface by,

$$B_s = B_c (r_{\text{cmb}} / R)^3 \quad (24)$$

and related to the magnetic moment by,

$$\mu = 4\pi r_{\text{cmb}}^3 B_c / \sqrt{2} \mu_0 \quad (25)$$

which is an intrinsic and directly measurable property of a planetary dynamo. For the Earth model described in Section 3.5, using  $\gamma_d = 0.17$ , we find  $\mu = 83 \text{ ZA m}^2$ ,  $B_c = 0.27 \text{ mT}$ , and  $B_s = 0.032 \text{ mT}$ , which are similar to present-day measurements of the geomagnetic dipole field.

#### 4.2. Alternative dynamo energy sources

Thermal convection is one of several energy sources that can drive a planetary dynamo. However, thermal convection has many advantages. Here we discuss why three alternative energy sources, compositional convection, radioactive heating, and external forcing, are less important than thermal convection for maintaining a strong dynamo.

Compositional convection requires that the core geotherm cross the solidus and that the core fluid contain an incompatible light element. However, the buoyancy flux in the core associated with thermal gradients has the potential to be much larger than those of compositional gradients, particularly when the core heat flow is large. This is demonstrated in thermal history models that include the growth of the inner core ([Nimmo et al., 2004](#)) where the boost in entropy production of  $\sim 200 \text{ MW K}^{-1}$  associated with the onset of compositional convection ( $\sim 1 \text{ Ga}$ ) is much smaller than the initial ( $\sim 4 \text{ Ga}$ ) entropy production of  $\sim 1600 \text{ MW K}^{-1}$  associated with the rapid cooling of a completely liquid core. Also, a high compositional buoyancy flux implies that the core is solidifying quickly, which will decrease the volume of conductive fluid, the length scale of the dynamo region, and ultimately lead to complete core solidification.

Radioactive heating in the core due to the decay of  $K_{40}$  may account for about 25% of the present convective core heat flux and even more early in Earth history ([Nimmo, 2007](#)). Mathematically radioactive heating enters the energy balance like a secular cooling term, so in effect it has already been taken into account in the optimization. Including radioactivity in the core of an optimal planet will heat the core but not increase the temperature at the CMB because it is already at the maximum (solidus) value. In the optimal model the mantle is accepting as much core heat as possible, so

any additional heating of the core that cannot be conducted through the lower mantle thermal boundary layer will contribute to a hot and thermally stratified layer at the top of the core, likely inhibiting dynamo action.

External forcing in the form of precession or tides has a small influence, if any, on core flow ([Tilgner, 2007](#)). Maintaining dynamo action in a liquid core solely by external forcing is difficult because it must overcome any thermal stratification, maintain an adiabatic state in the core, and drive fluid motions beyond the threshold for both convection and dynamo action. Strong gravitational tides may in fact inhibit dynamo action, as may be the case for Io, if tidal dissipation heats the mantle enough to prevent the core from cooling ([Stevenson, 2010](#)).

In summary, although the three sources of buoyancy mentioned here can contribute to the dynamo, they rely on very specific thermo-chemical or dynamical scenarios and may even inhibit dynamo action in some cases. On the contrary, all planetary cores likely begin in a very hot state and the only requirement for thermally driven dynamo action is that they cool fast enough.

## 5. Results

For each combination of total planet mass and core-mass fraction we create a whole planet thermal profile by iterating between the internal structure model with a fixed temperature profile and the optimal thermal model with a fixed internal structure until additional iterations produce negligible changes in both. The last step is to apply the magnetic field scaling law.

### 5.1. Internal structure

[Fig. 2](#) shows the density (2a and b) and pressure (2c and d) profiles for 32% and 65% CMF and 1–10 $M_E$  optimal models, along with the present-day Earth model (labeled E) for comparison. The density jump in the Earth model associated with the ICB is the only visible departure from the optimal 1 $M_E$  model, the later being too hot to freeze out a solid inner core. In fact, for all optimal models the core is entirely liquid. In the Earth, solidification of the inner core provides a release of light elements at the ICB that is an additional source of energy available to drive core convection. Light element buoyancy production at the ICB is estimated to provide at least one half of the entropy available to drive the geodynamo ([Gubbins et al., 2004](#)) and is about twice as thermodynamically efficient than thermal buoyancy ([Roberts et al., 2003](#)). The absence of inner core solidification in the optimal models requires that core convection and dynamo action be maintained by thermal convection alone.

Although the cores are larger in the 65% CMF models, the surface radii are smaller because the iron core is much more dense than the silicate mantle. The density jumps in the optimal models in [Fig. 2](#) are associated with the pressure induced silicate phase transitions in the mantle and the silicate–iron interface at the CMB.

### 5.2. Mantle convection

Optimal whole planet temperature profiles are shown in [Fig. 3](#). In general, the CMB temperature is hotter in the 32% CMF models than those with larger cores because the melting law in (16) is proportional to  $P_{\text{cmb}}$ , which is larger in 32% CMF models because the CMB is deeper. The optimal Earth-mass model is hotter than the Earth model (bottom curve in [Fig. 3a](#)) because the CMB temperature of the Earth is considerably lower than the melting temperature for perovskite. The mid-mantle temperature in the Earth model is nearly as hot as in the optimal model due to internal heat production.

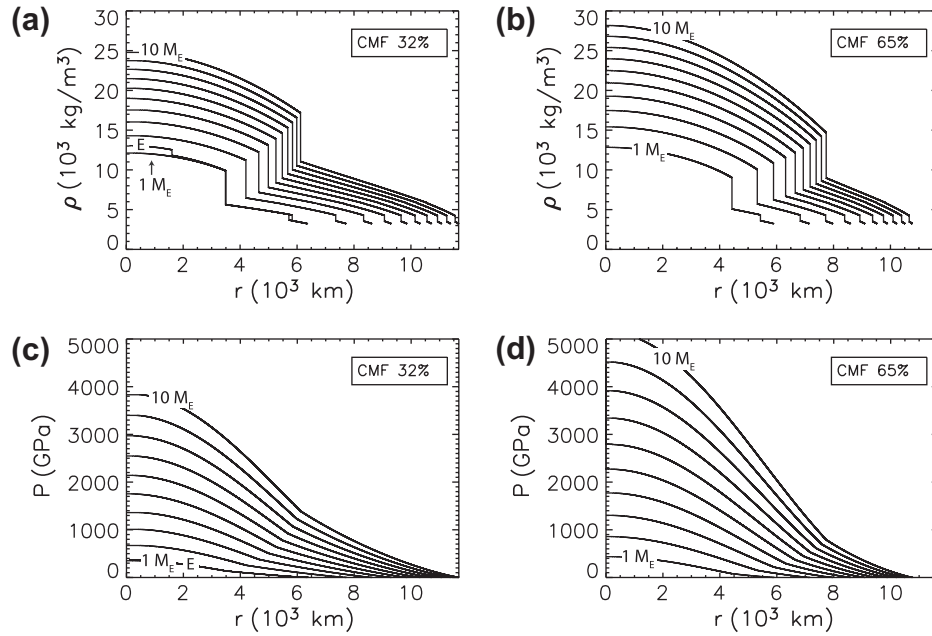


**Fig. 2.** Radial structure profiles for 1–10 $M_E$  optimal models and the Earth model (labeled E). (a) Density profiles for 32% core-mass fraction (CMF). (b) Density profiles for 65% CMF. (c) Pressure profiles for 32% CMF. (d) Pressure profiles for 65% CMF. Note that the Earth model density profile overlaps with the optimal  $1M_E$  model, except for the jump in the Earth model at the inner core boundary. The Earth model pressure profile is indistinguishable from the optimal  $1M_E$  model.

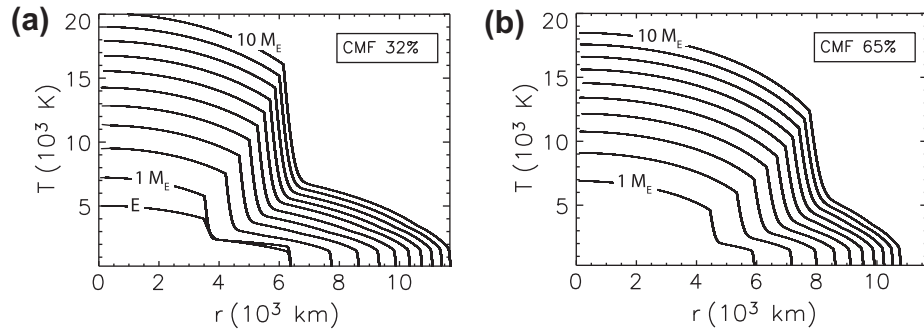


**Fig. 3.** Temperature profiles for 1–10 $M_E$  optimal models and the Earth model (labeled E). (a) 32% core-mass fraction (CMF). (b) 65% CMF.

Thermal properties for the upper and lower mantle boundary layers are shown in Figs. 4 and 5, respectively. The optimal surface heat flow is only constrained by the upper mantle melting curve and the critical local Rayleigh number assumption. These constraints limit  $\Delta T_1$  in the range 1100–1300 K and  $\delta_1$  in the range 60–40 km. However, since  $T_{cmb}$  increases with planet mass, most of the convective temperature increase needed to reach  $T_{cmb}$  must occur in the lower mantle thermal boundary layer. The surface heat flow  $Q_1$  (Fig. 4c) for the Earth model is similar to the Earth-mass optimal model because the upper mantle thermal boundary layer is close to the optimal state as defined here. Also,  $Q_1$  is slightly larger for the 32% CMF models due to a larger surface area, despite the fact that the average surface heat flux ( $q_1 = Q_1/A_1$ ) is larger for 65% CMF. Fig. 4d confirms that the Rayleigh number in the upper mantle  $Ra_1$  is set to  $Ra_{crit}$  in the optimal models.

Fig. 5 shows the thermal properties of the lower mantle boundary layer. As expected, the temperature jump  $\Delta T_2$  is larger and varies more with mass than  $\Delta T_1$  because of the dependence of  $T_{cmb}$  on pressure. The lower boundary layer thickness is a free parameter that is constrained by the CMB heat flow according to (21), and varies in proportion to  $\Delta T_2$ . The Rayleigh number in the lower boundary layer  $Ra_2$  is larger than  $Ra_1$  because it increases as  $\sim \Delta T_2 \delta_2^3$ . We note that in the calculation of  $Ra_2$  we have assumed

that  $\alpha g / \nu \kappa$  is equal in the two boundary layers, but a systematic increase in  $\nu$  in the lower mantle of order  $\sim 10^3$  (as is thought to occur in the Earth) would bring the value of  $Ra_2$  down closer to  $Ra_{crit}$ . Whole mantle Rayleigh numbers increase with mantle mass and are in the range  $3 \times 10^6$ – $5 \times 10^8$ , assuming  $\eta = 10^{21}$  Pa s,  $\alpha = 2 \times 10^{-5}$  K<sup>-1</sup>, and  $\kappa = 10^{-6}$  m<sup>2</sup> s<sup>-1</sup>. These Rayleigh numbers are similar to those in the Earth implying whole mantle convection, although the viscosity at such high pressures and temperatures is highly uncertain.

### 5.3. Surface age

A compelling feature of this model is the influence the upper mantle thermal boundary layer may have on the recycling rate of surface materials. In the mobile-lid regime, surface tectonics are connected to large scale mantle convection by a complex function of composition and rheology, which is not fully understood in the Earth (e.g. Schubert et al., 2001; Bercovici, 2003). If the optimal models described here produce surface tectonics similar to the Earth then we can say something about the typical time and length scales of surface processes.

In situ measurements of the Earth's oceanic crust show that for seafloor younger than 80 Myr the decrease in heat flux with mean

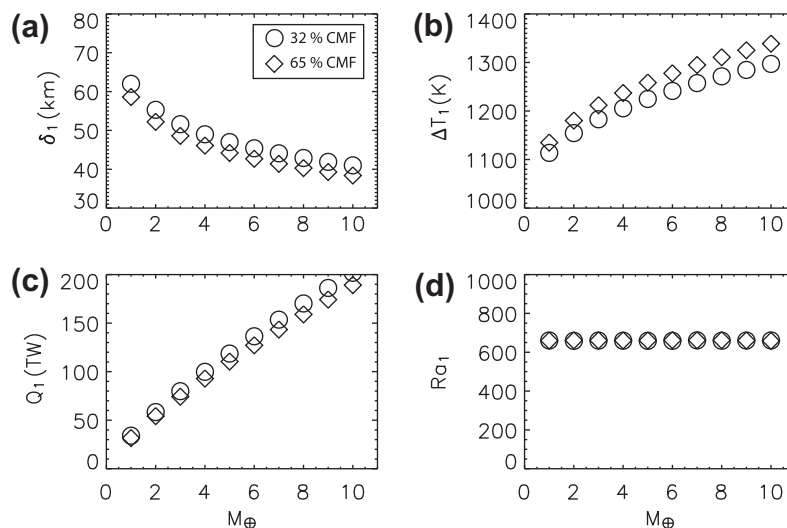


**Fig. 4.** Optimal thermal properties in the upper mantle boundary layer. Thermal boundary layer (a) thickness  $\delta_1$ , (b) temperature jump  $\Delta T_1$ , (c) surface heat flow  $Q_1$ , and (d) boundary layer Rayleigh number  $Ra_1$ .

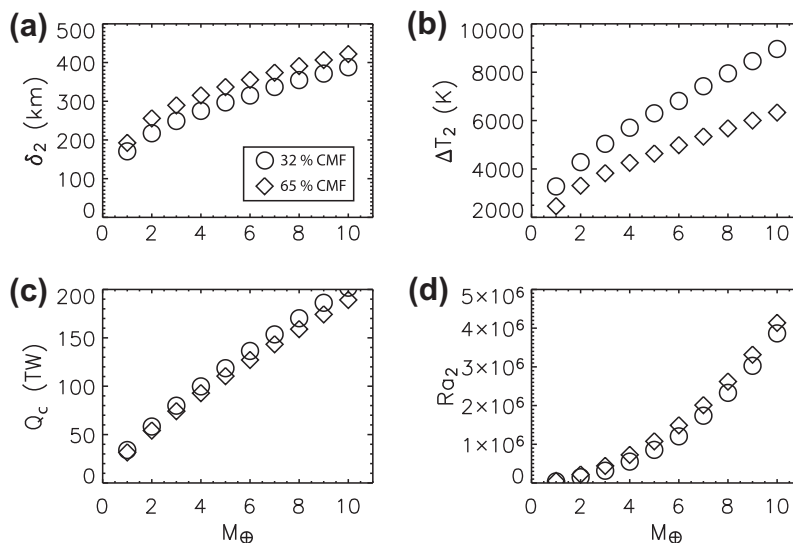


**Fig. 5.** Optimal thermal properties in the lower mantle boundary layer. Thermal boundary layer (a) thickness  $\delta_2$ , (b) temperature jump  $\Delta T_2$ , (c) CMB heat flow  $Q_c$ , and (d) boundary layer Rayleigh number  $Ra_2$ .

crustal age  $\tau$  is consistent with a simple half-space cooling model of the form  $q \propto \tau^{-1/2}$  (Jaupart et al., 2007). Physically this says that where the upper mantle thermal boundary layer is thicker the oceanic crust is older and colder. In the half-space cooling model, mean crustal age is equated with the thermal diffusion time through the conductive thermal boundary layer with thickness  $\delta_T$ . We assume this to be the same as the depth at which partial melting occurs and that the presence of water in the Earth's mantle depresses the melting curve, increasing this depth by 40% (Hirth and Kohlstedt, 1996; Karato and Jung, 1998). With  $\delta_T = 1.4\delta_1$  the mean crustal age as a function of the upper mantle boundary layer thickness is (Turcotte and Schubert, 2002),

$$\tau = \frac{(\delta_T/2)^2}{\kappa} \quad (26)$$

where  $\kappa = 10^{-6} \text{ m}^2 \text{ s}^{-1}$  is thermal diffusivity. If we further assume, for example, a convective planform with an average wavelength of  $\lambda = 2\pi R/m$ , where  $m = 5$  is the dominant mode of the planform, then we may estimate the mean surface velocity

$$u = \frac{\lambda/2}{\tau} \quad (27)$$

corresponding to a convection cell length of  $\lambda/2$ .

For the Earth model with  $\delta_T = 100 \text{ km}$ , (26) and (27) give  $\tau = 78 \text{ Myr}$ ,  $\lambda = 8000 \text{ km}$ , and  $u = 50 \text{ mm year}^{-1}$ , similar to present-day oceanic crust. When applied to the optimal models (Fig. 6) this predicts younger and faster plates on average compared to the Earth. We emphasize that this calculation is merely illustrative, and our model does not rely on some form of Earth-like plate tectonics being active at the surface, nor are we arguing that this should be the case, which is a topic of recent controversy (O'Neill et al., 2007; Valencia and O'Connell, 2009).

#### 5.4. Core convection

To maintain convective dynamo action in the core of a planet without a solidifying inner core the average CMB heat flow must exceed the adiabatic heat flux. The adiabatic heat flow from the

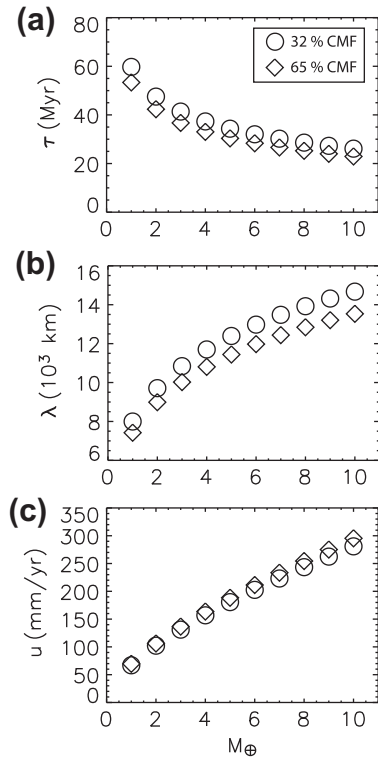


**Fig. 6.** Mobile-lid surface properties. (a) Mean surface age  $\tau$ . (b) Cell length  $\lambda$ . (c) Mean surface velocity  $u$ .

core is  $Q_{ad}$  and the super-adiabatic heat flow available to drive convection there is  $Q_{conv} = Q_c - Q_{ad}$ . The convective heat flow  $Q_{conv}$  is positive for all optimal models (Fig. 7), consistent with thermal convection in each case.  $Q_{conv}$  is larger in the 32% CMF models because they maintain a larger total heat flow at the core surface and require about half the adiabatic core heat flow of the 65% CMF models. The ratio  $Q_{conv}/Q_{ad}$  varies from 1 to 5 in the 32% CMF models, and from 0.3 to 2 in the 65% CMF models. Therefore, thermal convection is expected to be more rigorous in the 32% CMF models, although as we will see below the magnetic field strength is both a function of heat flux and size of the dynamo region, which is larger in the 65% CMF models.

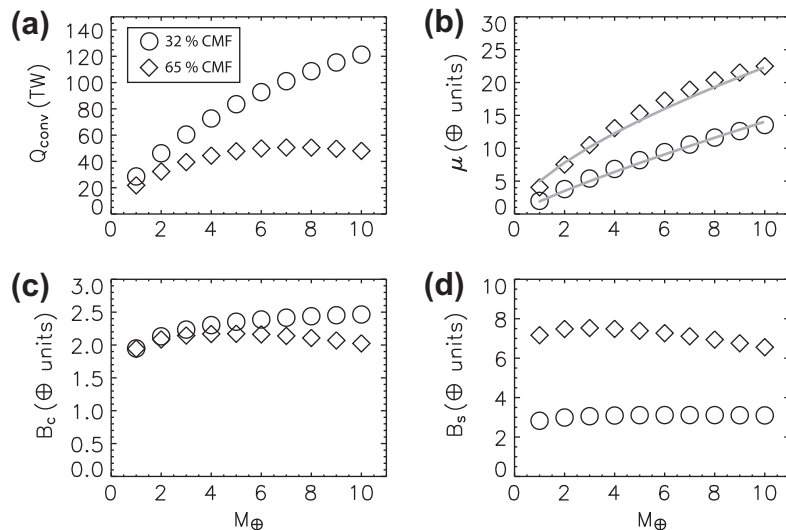


**Fig. 7.** Core convection and magnetic field properties. (a) Convective core heat flow  $Q_{conv}$ . (b) Magnetic moment  $\mu$ . (c) CMB magnetic field intensity  $B_c$ . (d) Planetary surface magnetic field intensity  $B_s$ . Geomagnetic units:  $\mu_{\oplus} = 78 \text{ ZA m}^2$ ,  $B_{c,\oplus} = 0.264 \text{ mT}$ ,  $B_{s,\oplus} = 30,300 \text{ nT}$ .

### 5.5. Core evolution

As the planet cools the core heat flow will decrease from the optimal heat flow estimated above. The secular cooling rate of the core is

$$-\frac{dT_c}{dt} = \frac{Q_c}{M_c c_p} \quad (28)$$

where  $T_c$  is the mean core temperature,  $M_c$  is core mass, and core heat capacity is  $c_p = 1000 \text{ J kg}^{-1} \text{ K}^{-1}$ . For 1–10 $M_E$  models with 32% CMF we find  $-dT_c/dt = 550\text{--}320 \text{ K Gyr}^{-1}$ , which corresponds to a fractional decrease of 35–10% in the core temperature over 4.5 Gyr, respectively. For models with a larger core fraction the secular cooling rate is about half as fast because planets with smaller cores tend to evolve faster.

Given these cooling rates we can estimate the time it would take an optimal core to begin to solidify. The temperature drop needed in the core to reach the iron solidus is  $\Delta T_s = T_{melt} - T_{cen}$ , where  $T_{cen}$  is the temperature and  $T_{melt}$  the iron solidus (11) both at the center of the core. If  $T_{cen}$  decreases at a rate  $\dot{T}_c$  given by (28) then we can estimate the time to solidification as  $\tau_s = \Delta T_s / \dot{T}_c$ . However, if the temperature drop needed to solidify the inner core  $\Delta T_s$  is greater than the lower mantle temperature jump  $\Delta T_2$ , then the core and mantle reach thermal equilibrium before inner core solidification. The only models that allow for inner core solidification have mass  $< 2M_E$ . For these 1–2 $M_E$  models, the times to solidification are 4.6–8.2 Gyr for 32% CMF, and 7.5–14.4 Gyr for 65% CMF, respectively. Therefore, thermal convection will be the dominant energy source available to drive dynamo action in almost all models. Gaidos et al. (2010) find similar results, namely that large planets do not cool fast enough to solidify an inner core and that dynamo action in the cores of these planets must be maintained by thermal convection.

### 5.6. Influence of radioactivity

Given that the presence of radioactive elements and secular cooling of the mantle are difficult to avoid, we estimate the effect of including a small amount of internal heating in the mantle  $Q_R$ . If  $Q_R$  is some fraction of the optimal surface heat flow  $Q_1$  then core heat flow must decrease by the same amount. Decreasing core heat flow by 10%, for example, will decrease the optimal dynamo magnetic field intensity by 4% according to (23). Assuming an

abundance of radioactivity in the convecting mantle similar to that of the present day Earth of  $H = 3.2 \times 10^{-12} \text{ W kg}^{-1}$  (Jaupart et al., 2007), radioactivity will account for  $\sim 50\%$  ( $\sim 25\%$ ) of the surface heat flow for 32% (65%) CMF optimal models. Core heat flow will decrease by the same amount, curtailing magnetic field strength and ultimately shutting the dynamo down altogether for  $\sim 7M_E$  planets.

### 5.7. Magnetic field

As demonstrated in Fig. 7a, the heat flux at the top of the core is super-adiabatic in all models and, assuming a fast Earth-like rotation rate, we expect a convecting iron core to maintain dynamo action and a large-scale dipolar magnetic field. As a check, we calculate the magnetic Reynolds number for each model using  $Rm = u_c r_{cmb} / \eta_m$ , where  $u_c$  is the convective velocity in the core and the magnetic diffusivity is  $\eta_m = 2 \text{ m}^2 \text{ s}^{-1}$  (Jones, 2007). We use a scaling relation (Olson and Christensen, 2006) to relate the convective velocity to the buoyancy flux

$$u_c \simeq 1.3 (r_{cmb} / \Omega)^{1/5} F^{2/5} \quad (29)$$

which gives strongly supercritical magnetic Reynolds numbers of  $Rm \sim 10^4$  for the optimal models. The same relation gives  $Rm \sim 2500$  for the geodynamo, which is about twice the typical estimates (Christensen and Tilgner, 2004) because the numerical coefficient in (29) is about twice as large for basal compared to internally heated dynamos.

To calculate the magnetic field intensity we use the scaling laws in (23)–(25), with  $\gamma_d = 0.2$ . Fig. 7 shows the magnetic moment  $\mu$  (7b), and the magnetic field at the top of the core  $B_c$  (7c) and planet surface  $B_s$  (7d), in geomagnetic units. A scaling law is plotted (grey) for the magnetic moment as a function of mass and CMF of the form,

$$\mu = \mu_1 (\text{CMF}/0.32)^{c_1} (M/M_E)^{c_2} \quad (30)$$

where  $\mu_1$  is the magnetic moment of the optimal Earth-mass model, and the exponents are  $c_1 = 1.3$ , and  $c_2 = 0.85$  or  $0.65$  for the 32% or 65% CMF models, respectively. A similar scaling law for the planet radius is constructed with exponents  $c_1 = -0.12$  and  $c_2 = 0.27$ .

Magnetic field intensity at the CMB is slightly stronger for 32% CMF because of a higher convective heat flow, but  $B_c$  is confined to a modest 2–2.5 times the geomagnetic field strength for all cases. For larger cores the dynamo region is closer to the planetary surface so  $B_s$  exceeds the 32% CMF surface fields by about a factor of 2.5. Magnetic moment is a strong function of core size and varies up to 23 times the geomagnetic dipole moment for a  $10M_E$  planet with a large core. According to the trends in Fig. 7 we expect little change in the magnetic field intensity at the CMB and only modest increases in  $\mu$  for even larger planet masses and cores than those considered here. However, important material properties, such as viscosity and thermal conductivity, at ultra high pressures and temperatures are so uncertain that extrapolation to even higher pressures and temperatures becomes questionable.

## 6. Detectability

The magnetic fields of the giant planets in the Solar System were first remotely detected by their electron cyclotron emission at radio frequencies. In fact, the oscillation of such emissions caused by non-axisymmetric field components is commonly used to define the rotation periods of the gas planets, whose surfaces rotate differentially (Guillot, 2005; Gurnett et al., 2007). Predictions of radio emission from extrasolar magnetic fields (Yantis et al., 1977; Lecacheux, 1991) predate the detection of the first exoplanet in 1995.

Electron cyclotron emission is caused by energetic solar wind electrons interacting with planetary magnetic field lines, generating radiation at the electron cyclotron frequency

$$f_c = eB_s / 2\pi m_e \quad (31)$$

where  $e$  and  $m_e$  are electron charge and mass. These electrons are typically concentrated near the magnetic poles where the field is strongest so emission is expected to be pronounced along the axis of the dipole field. Emission power is observed to depend on solar wind intensity and planetary magnetic field strength. Desch and Kaiser (1984) developed an empirical scaling law (the so-called “Radiometric Bodes Law”) for emission power as a function of magnetic moment and orbital distance for the magnetic planets in the Solar System. We use a version of this law of the form,

$$P_{rad} = \left( \frac{\mu}{\mu_J} \right)^{0.58} \left( \frac{a_J}{a} \right)^{1.17} \times 4 \times 10^9 \text{ W} \quad (32)$$

where  $a$  is semi-major axis, subscript  $J$  refers to Jupiter, and the constant coefficient on the right is proportional to the intensity of the solar wind (Farrell et al., 1999). The radio flux observed at the Earth is the emission power divided by the spherical area of projection,

$$\Phi = P_{rad} / 4\pi s^2 \Delta f \quad (33)$$

where  $s$  is the distance to the planet from Earth and  $\Delta f$  is the observational bandwidth, assumed here to be  $f_c/2$ . Low frequency planetary emissions may be of similar magnitude to stellar emissions and discernible based on the polarization of their radiation (Zarka, 2007).

Fig. 8 shows the cyclotron emission power versus frequency for a number of terrestrial exoplanets assuming they are in an optimal state and have a large 65% core-mass fraction. The exoplanets shown, GJ674b ( $11.7M_E$ ), GJ581b ( $15.6M_E$ ), GJ581e ( $1.94M_E$ ), 55Cnc e ( $7.63M_E$ ), and HD7924b ( $9.22M_E$ ), all orbit within  $a = 0.1$  AU and are less than  $s = 17$  pc away (see Schneider, 2010). Fig. 8 also shows the potential emission from exoplanets with 1– $10M_E$  and 32% or 65% CMF orbiting at  $a = 0.02$  AU around the stars GJ876 ( $s = 4.72$  pc) and  $\alpha$  Centauri ( $s = 1.33$  pc), and the emission from Earth, Jupiter, and Saturn if they orbited  $\alpha$  Centauri. Due to the fact that the Earth’s ionosphere blocks emissions with

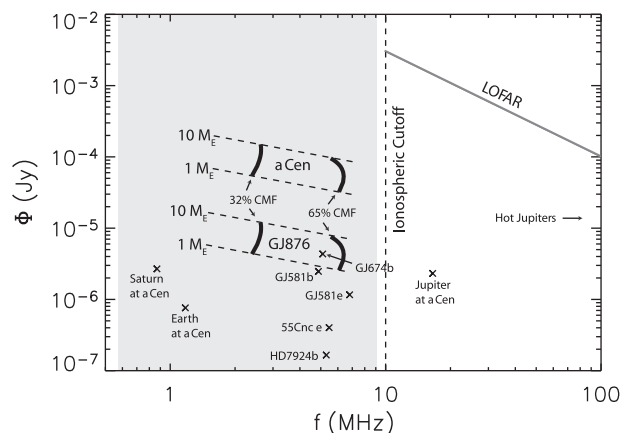


**Fig. 8.** Cyclotron radio emission spectrum for optimal 32% and 65% CMF exoplanets. Shaded region indicates the terrestrial dynamo region for cyclotron emission. Solid curves are the emission from 1– $10M_E$  optimal exoplanets orbiting at  $a = 0.02$  AU around  $\alpha$  Centauri at  $s = 1.33$  pc and GJ876 at  $s = 4.72$  pc from Earth. Also shown are the expected emissions for nearby exoplanets GJ674b, GJ581b, GJ581e, 55Cnc e, and HD7924b all assuming 65% CMF, and for Earth, Jupiter, and Saturn analogs assuming they orbit  $\alpha$  Centauri. The ionospheric cutoff at 10 MHz sets the lower frequency limit for ground-based radio telescopes such as LOFAR, shown for an 8 h exposure detection threshold.

frequencies less than  $f_i \approx 10$  MHz, detection of exo-magnetic fields requires that the radio observations occur at night, in polar regions ( $f_i \approx 3$  MHz), or above the ionosphere entirely. However, if intrinsic magnetic field intensities vary by a factor of  $\sim 3$  similar to paleointensity records of the geomagnetic field, then exoplanet magnetic fields may temporarily emit at frequencies higher than  $f_i$ . The detection power threshold expected for the Low Frequency Array (LOFAR), the most sensitive ground-based radio telescope (Kassim et al., 2004), for an 8 h observing time is  $\sim 1$  mJy near 10 MHz.

Cyclotron emission power is expected to increase with stellar wind density and velocity, so that stellar flares should provide a temporary burst of cyclotron emission from the planet. The closest stars are generally chromospherically quiet like the Sun, so that periodically flaring or younger more active stars, although more distant, may be better targets. Alternative boosts and modulations to the emission amplitude may be generated by a highly eccentric orbit, where solar wind intensity would be a maximum at periastron, or by interaction with another nearby magnetic planet. For example, there is a periodic modulation of Jupiter's decametric emission at the orbital period of Io due to a uni-polar magnetic interaction between the jovian field and the moon (Zarka, 2007). In dynamically crowded planetary systems like GJ876 interaction between multiple planetary magnetic fields may also modulate the emission at regular, resonant intervals.

Is it possible to detect the magnetic field of a terrestrial exoplanet? For the cyclotron frequency to be at least equal to the ionospheric cutoff frequency of 10 MHz the surface magnetic field must be at least  $B_s = 384 \mu\text{T}$ , which is about ten times the strength of the geomagnetic field. The upper limit we predict for a  $10M_E$  planet with a large core is  $B_s \approx 200 \mu\text{T}$  with cyclotron frequency  $f_c \approx 5.5$  MHz. To ensure that the ionosphere does not interfere we will assume this dynamo is in an anomalously strong field state three times its average intensity, giving  $f_c \approx 16.5$  MHz. If the planet orbits Alpha Centauri at 0.1 AU this implies a radio emission power of  $9.6 \times 10^{-6}$  Jy. To be detectable with LOFAR the emission power would need to be increased by a factor of at least  $10^3$ . Such a boost is possible through a combination of a stellar wind burst, which can boost the radio power by a factor of  $\sim 10^2$ , and a concentrated cyclotron beam, which can boost the emission flux by a factor of 130 for a beam of width  $\sim 10^\circ$  (Farrell et al., 1999). For GJ581e the same analysis predicts a flux of  $7.3 \times 10^{-7}$  Jy at  $f_c = 20.4$  MHz, which may also be temporarily detectable with these boosts.

Several groups are currently searching for magnetospheric emissions from hot-Jupiter exoplanets, which are expected to have stronger magnetic fields and emit at higher frequencies (e.g. Farrell et al., 2004; Lazio et al., 2010). Although no emission from an exoplanet magnetic field has yet been found, the lower limits of the observable emission power are approaching the range predicted by dynamo theory for such planets.

## 7. Summary and conclusions

With the hope of one day detecting the magnetic field of a terrestrial exoplanet we have defined an optimal whole planet thermal state that maximizes core heat loss and estimated the corresponding dynamo magnetic field intensity. The model assumes that the local Rayleigh number is critical for convection in the upper mantle thermal boundary layer, that the temperature profile is at the solidus in the boundary layers, and that internal heating is negligible in the mantle. We apply this optimal state to internal structure models for  $1\text{--}10M_E$  terrestrial planets with a 32% or 65% core-mass fraction. We find that these planets can produce surface magnetic fields that are 2–5 times stronger than the geomagnetic field, and magnetic dipole moments 2–23 times the geomagnetic dipole moment. Since these models have been

constructed to be optimal for magnetic field generation, they likely represent an upper limit on the magnetic field intensities of a thermally driven dynamo. Additional energy sources that increase the energy flux through the core may boost the magnetic field strength further, but require special conditions.

Cyclotron radio emission from nearby magnetic exoplanets may be detectable in the future, although the nominal cyclotron emission frequency of terrestrial-type magnetic fields is likely below the Earth's ionospheric cutoff frequency. In general, stronger magnetic fields emit more intensely so the most promising targets would be those in an optimal dynamo configuration with a combination of driving sources and dynamics that maximize the magnetic field intensity. To this end, quantitative predictions of exoplanet magnetic field intensities and cyclotron emission can guide observers to the most promising targets. Additional boosts of the cyclotron emission, for example caused by intrinsic magnetic field fluctuations, stellar flares, eccentric orbits, or interactions with nearby magnetic planets, may be essential to their detection.

## Acknowledgements

This paper benefited from discussions with Darrell Strobel, Ulrich Christensen, Joseph Lazio, and Dave Bercovici. We thank two anonymous reviewers for their detailed and insightful comments that greatly improved this manuscript.

## References

- Alfe, D., Gillan, M., Price, G., 2003. A thermodynamics from first principles: Temperature and composition of the Earth's core. *Mineral. Mag.* 67 (1), 113–123.
- Anderson, J., Schubert, G., 2007. Saturn's gravitational field, internal rotation, and interior structure. *Science* 317 (5843), 1384–1387.
- Bercovici, D., 2003. The generation of plate tectonics from mantle convection. *Earth Planet. Sci. Lett.* 205 (3–4), 107–121.
- Boehler, R., 2007. Properties of Rocks and Minerals – High-Pressure Melting. *Treatise on Geophysics*, vol. 2. Elsevier, Amsterdam (Chapter 18).
- Boehler, R., Bagen, V., Chopelas, A., 1990. Melting, thermal expansion, and phase transitions of iron at high pressures. *J. Geophys. Res.* 95, 21731–21736.
- Chopelas, A., Boehler, R., 1992. Thermal expansivity in the lower mantle. *Geophys. Res. Lett.* 19 (19), 1983–1986.
- Christensen, U., Aubert, J., 2006. Scaling properties of convection-driven dynamos in rotating spherical shells and application to planetary magnetic fields. *Geophys. J. Int.* 166 (1), 97–114.
- Christensen, U., Tilgner, A., 2004. Power requirement of the geodynamo from ohmic losses in numerical and laboratory dynamos. *Nature* 429 (6988), 169–171.
- Christensen, U.R., Schmitt, D., Rempel, M., 2008. Planetary dynamos from a solar perspective. *Space Sci. Rev.* doi:10.1007/s11214-008-9449-6.
- Christensen, U., Holzwarth, V., Reiners, A., 2009. Energy flux determines magnetic field strength of planets and stars. *Nature* 457, 167–169.
- Conrad, C., Molnar, P., 1999. Convective instability of a boundary layer with temperature- and strain-rate-dependent viscosity in terms of available buoyancy. *Geophys. J. Int.* 139 (1), 51–68.
- Dehant, V., Lammer, H., Kulikov, Y., Grießmeier, J., Breuer, D., Verhoeven, O., Karatekin, Ö., Van Hoolst, T., Korabely, O., Lognonné, P., 2007. Planetary magnetic dynamo effect on atmospheric protection of early Earth and Mars. *Space Sci. Rev.* 129 (1), 279–300.
- Desch, M., Kaiser, M., 1984. Predictions for Uranus from a radiometric Bode's law. *Nature* 310, 755–757.
- Dziewonski, A., Anderson, D., 1981. Preliminary reference Earth model. *Phys. Earth Planet. Inter.* 25 (4), 297–356.
- Elsasser, W., 1946. Induction effects in terrestrial magnetism: Part II. The secular variation. *Phys. Rev.* 70 (3–4), 202–212.
- Farrell, W., Desch, M., Zarka, P., 1999. On the possibility of coherent cyclotron emission from extrasolar planets. *J. Geophys. Res.* 104 (E6).
- Farrell, W., Lazio, T., Zarka, P., Bastian, T., Desch, M., Ryabov, B., 2004. The radio search for extrasolar planets with LOFAR. *Planet. Space Sci.* 52 (15), 1469–1478.
- Fischer, D., 2008. Mapping the realm of hot Jupiters. *Phys. Scr.* 130, 014002-1–8.
- Gaidos, E., Conrad, C., Manga, M., Hernlund, J., 2010. Thermodynamic limits on magnetodynamos in rocky exoplanets. *Astrophys. J.* 718, 596–609.
- Griessmeier, J., Stadelmann, A., Penz, T., Lammer, H., Selsis, F., Ribas, I., Guinan, E., Motschmann, U., Biernat, H., Weiss, W., 2004. The effect of tidal locking on the magnetospheric and atmospheric evolution of “Hot Jupiters”. *Astron. Astrophys.* 425 (2), 753–762.
- Gubbins, D., Alfe, D., Masters, G., Price, G., Gillan, M., 2004. Gross thermodynamics of two-component core convection. *Geophys. J. Int.* 157 (3), 1407–1414.

- Guillot, T., 2005. The interiors of giant planets: Models and outstanding questions. *Annu. Rev. Earth Planet. Sci.* 33, 493–530.
- Gurnett, D., Persoon, A., Kurth, W., Groene, J., Averkamp, T., Dougherty, M., Southwood, D., 2007. The variable rotation period of the inner region of Saturn's plasma disk. *Science* 316 (5823), 442–445.
- Hernlund, J.W., Labrosse, S., 2007. Geophysically consistent values of the perovskite to post-perovskite transition Clapeyron slope. *Geophys. Res. Lett.* 34, L05309-1–4.
- Hirschmann, M., 2000. Mantle solidus: Experimental constraints and the effects of peridotite composition. *Geochem. Geophys. Geosyst.* 1 (10), 1042–1–26.
- Hirth, G., Kohlstedt, D., 1996. Water in the oceanic upper mantle: Implications for rheology, melt extraction and the evolution of the lithosphere. *Earth Planet. Sci. Lett.* 144 (1–2), 93–108.
- Hofmeister, A., 1999. Mantle values of thermal conductivity and the geotherm from phonon lifetimes. *Science* 283 (5408), 1699–1706.
- Holland, K., Ahrens, T., 1997. Melting of (Mg,Fe)<sub>2</sub>SiO<sub>4</sub> at the core–mantle boundary of the Earth. *Science* 275 (5306), 1623–1625.
- Howard, A., Marcy, G., Johnson, J., Fischer, D., Wright, J., Isaacson, H., Valenti, J., Anderson, J., Lin, D., Ida, S., 2010. The occurrence and mass distribution of close-in super-Earths, Neptunes, and Jupiters. *Science* 330 (6004), 653–655.
- Ida, S., Lin, D., 2004. Toward a deterministic model of planetary formation. I. A desert in the mass and semimajor axis distributions of extrasolar planets. *Astrophys. J.* 604 (1), 388–413.
- Ito, E., Takahashi, E., 1989. Postspinel transformations in the system Mg<sub>2</sub>SiO<sub>4</sub>–Fe<sub>2</sub>SiO<sub>4</sub> and some geophysical implications. *J. Geophys. Res.* 94, 10637–10646.
- Jaupart, C., Labrosse, S., Mareschal, J.C., 2007. Temperatures, Heat and Energy in the Mantle of the Earth. *Mantle Dynamics of Treatise on Geophysics*, vol. 7. Elsevier, Amsterdam. pp. 253–305 (Chapter 2).
- Jones, C.A., 2007. Thermal and Compositional Convection in the Outer Core. *Treatise on Geophysics*, vol. 8. Elsevier, Amsterdam. pp. 131–185.
- Karato, S., Jung, H., 1998. Water, partial melting and the origin of the seismic low velocity and high attenuation zone in the upper mantle. *Earth Planet. Sci. Lett.* 157 (3–4), 193–207.
- Kassim, N., Lazio, T., Ray, P., Crane, P., Hicks, B., Stewart, K., Cohen, A., Lane, W., 2004. The low-frequency array (LOFAR): Opening a new window on the universe. *Planet. Space Sci.* 52 (15), 1343–1349.
- Lammer, H. et al., 2007. Coronal mass ejection (CME) activity of low mass M stars as an important factor for the habitability of terrestrial exoplanets. II. CME-induced ion pick up of Earth-like exoplanets in close-in habitable zones. *Astrobiology* 7 (1), 185–207.
- Lammer, H., Kasting, J., Chassefière, E., Johnson, R., Kulikov, Y., Tian, F., 2008. Atmospheric escape and evolution of terrestrial planets and satellites. *Space Sci. Rev.* 139 (1), 399–436.
- Laughlin, G., Bodenheimer, P., Adams, F., 2004. The core accretion model predicts few jovian-mass planets orbiting red dwarfs. *Astrophys. J.* 612 (1), 73–76.
- Lavorel, G., Le Bars, M., 2010. Experimental study of the interaction between convective and elliptical instabilities. *Phys. Fluids* 22, 114101-1–8.
- Lay, T., Hernlund, J., Garnero, E., Thorne, M., 2006. A post-perovskite lens and D' heat flux beneath the central Pacific. *Science* 314 (5803), 1272–1276.
- Lazio, T., Carmichael, S., Clark, J., Elkins, E., Gudmundsen, P., Mott, Z., Szwajkowski, M., Hennig, L., 2010. Planetary magnetospheric emission survey. *Astron. J.* 139, 96–101.
- Lecacheux, A., 1991. On the feasibility of extra-solar planetary detection at very low radio frequencies. In: Heidmann, J., Klein, M. (Eds.), *Proceedings of Bioastronomy, the Search for Extraterrestrial Life*. Springer, pp. 21–30.
- Lin, J., Campbell, A., Heinz, D., Shen, G., 2003. Static compression of iron–silicon alloys: Implications for silicon in the Earth's core. *J. Geophys. Res.* 108 (B1), 11.
- Merkel, S., Goncharov, A., Mao, H., Gillet, P., Hemley, R., 2000. Raman spectroscopy of iron to 152 gigapascals: Implications for Earth's inner core. *Science* 288 (5471), 1626–1629.
- Mosenfelder, J., Asimow, P., Ahrens, T., 2007. Thermodynamic properties of Mg<sub>2</sub>SiO<sub>4</sub> liquid at ultra-high pressures from shock measurements to 200 GPa on forsterite and wadsleyite. *J. Geophys. Res.* 112, B06208-1–13.
- Nimmo, F., 2002. Why does Venus lack a magnetic field? *Geology* 30 (11), 987–990.
- Nimmo, F., 2007. Energetics of the core. In: Olson, P. (Ed.), *Core Dynamics*. Treatise on Geophysics, vol. 8. Elsevier, Amsterdam, pp. 31–66 (Chapter 2).
- Nimmo, F., Price, G., Brodholt, J., Gubbins, D., 2004. The influence of potassium on core and geodynamo evolution. *Geophys. J. Int.* 156 (2), 363–376.
- Oganov, A., 2007. Theory and practice – Thermodynamics, equations of state, elasticity, and phase transitions of minerals at high pressures and temperatures. In: Schubert, G. (Ed.), *Treatise on Geophysics*. Elsevier, Amsterdam, pp. 121–152.
- Olson, P., Christensen, U., 2006. Dipole moment scaling for convection-driven planetary dynamos. *Earth Planet. Sci. Lett.* 250 (3–4), 561–571.
- Olson, P., Driscoll, P., Amit, H., 2009. Dipole collapse and reversal precursors in a numerical dynamo. *Phys. Earth Planet. Inter.* 173, 121–140.
- O'Neill, C., Jellinek, A.M., Lenardic, A., 2007. Conditions for the onset of plate tectonics on terrestrial planets and moons. *Earth Planet. Sci. Lett.* 261 (1–2), 20–32.
- Paulson, A., Zhong, S., Wahr, J., 2005. Modelling post-glacial rebound with lateral viscosity variations. *Geophys. J. Int.* 163 (1), 357–371.
- Poirier, J., 1991. *Introduction to the Physics of the Earth's Interior*. Cambridge University Press.
- Roberts, P.H., 2007. *Theory of the Geodynamo*. Treatise on Geophysics, vol. 8. Elsevier, Amsterdam (Chapter 3).
- Roberts, P.H., Jones, C.A., Calderwood, A.R., 2003. Energy fluxes and ohmic dissipation in the Earth's core. *Earth's Core and Lower Mantle*. Taylor & Francis. pp. 100–129 (Chapter 5).
- Sanchez-Lavega, A., 2004. The magnetic field in giant extrasolar planets. *Astrophys. J.* 609 (2), 87–90.
- Schneider, J., 2010. *The Extrasolar Planets Encyclopedia*. <[www.exoplanet.eu](http://www.exoplanet.eu)>.
- Schubert, G., Turcotte, D., Olson, P., 2001. *Mantle Convection in the Earth and Planets*. Cambridge Univ. Press, New York.
- Seager, S., Kuchner, M., Hier-Majumder, C., Militzer, B., 2007. Mass–radius relationships for solid exoplanets. *Astrophys. J.* 669 (2), 1279–1297.
- Shim, S., 2008. The postperovskite transition. *Annu. Rev. Earth Planet. Sci.* 36, 569–599.
- Shkolnik, E., Bohlender, D., Walker, G., Collier Cameron, A., 2008. The on/off nature of star–planet interactions I. *Astrophys. J.* 676 (1), 628–638.
- Sotin, C., Grasset, O., Mocquet, A., 2007. Mass–radius curve for extrasolar Earth-like planets and ocean planets. *Icarus* 191 (1), 337–351.
- Stacey, F., 1992. *Physics of the Earth*. Brookfield Press, Brisbane, Australia.
- Stacey, F., Davis, P., 2004. High pressure equations of state with applications to the lower mantle and core. *Phys. Earth Planet. Inter.* 142 (3–4), 137–184.
- Stacey, F., Loper, D., 2007. A revised estimate of the conductivity of iron alloy at high pressure and implications for the core energy balance. *Phys. Earth Planet. Inter.* 161 (1–2), 13–18.
- Stevenson, D., 2001. Mars' core and magnetism. *Nature* 412 (6843), 214–219.
- Stevenson, D., 2010. Planetary magnetic fields: Achievements and prospects. *Space Sci. Rev.* 152 (1–4), 651–664.
- Stixrude, L., Lithgow-Bertelloni, C., 2005. Thermodynamics of mantle minerals – I. Physical properties. *Geophys. J. Int.* 162 (2), 610–632.
- Tilgner, A., 2007. *Rotational Dynamics of the Core*. Treatise on Geophysics, vol. 8. Elsevier, Amsterdam.
- Turcotte, D., Schubert, G., 2002. *Geodynamics*. Cambridge University Press.
- Uchida, T., Wang, Y., Rivers, M., Sutton, S., 2001. Stability field and thermal equation of state of e-iron determined by synchrotron X-ray diffraction in a multianvil apparatus. *J. Geophys. Res.* 106 (B10), 21799–21810.
- Valencia, D., O'Connell, R., 2009. Convection scaling and subduction on Earth and super-Earths. *Earth Planet. Sci. Lett.* 286 (3–4), 492–502.
- Valencia, D., O'Connell, R., Sasselov, D., 2006. Internal structure of massive terrestrial planets. *Icarus* 181 (2), 545–554.
- Van den Berg, A., Yuen, D., Allwardt, J., 2002. Non-linear effects from variable thermal conductivity and mantle internal heating: Implications for massive melting and secular cooling of the mantle. *Phys. Earth Planet. Inter.* 129 (3), 359–376.
- Van der Hilst, R., de Hoop, M., Wang, P., Shim, S., Ma, P., Tenorio, L., 2007. Seismostratigraphy and thermal structure of Earth's core–mantle boundary region. *Science* 315 (5820), 1813–1817.
- Vinet, P., Rose, J., Ferrante, J., Smith, J., 1989. Universal features of the equation of state of solids. *J. Phys.: Condens. Matter* 1, 1941–1963.
- Weast, R., 2009. *Handbook of Chemistry and Physics*, 89th ed. <<http://www.hbcpnetbase.com/>>.
- Yantis, W., Sullivan III, W., Erickson, W., 1977. A search for extra-solar jovian planets by radio techniques. *Bull. Am. Astron. Soc.* 9, 453.
- Zapolsky, H., Salpeter, E., 1969. The mass–radius relation for cold spheres of low mass. *Astrophys. J.* 158, 809–813.
- Zarka, P., 2007. Plasma interactions of exoplanets with their parent star and associated radio emissions. *Planet. Space Sci.* 55 (5), 598–617.
- Zarka, P., Treumann, R., Ryabov, B., Ryabov, V., 2001. Magnetically-driven planetary radio emissions and application to extrasolar planets. *Astrophys. Space Sci.* 277 (1), 293–300.
- Zerr, A., Diegeler, A., Boehler, R., 1998. Solidus of Earth's deep mantle. *Science* 281 (5374), 243–246.